JOURNAL OF GEOPHYSICAL RESEARCH, VOL. 115, D09106, doi:10.1029/2009JD013224, 2010

Meteorology and surface energy fluxes in the 2005–2007 ablation seasons at the Miage debris-covered glacier, Mont Blanc Massif, Italian Alps

Ben W. Brock,[1] Claudia Mihalcea,[2] Martin P. Kirkbride,[1] Guglielmina Diolaiuti,[2] Mark E. J. Cutler,[1] and Claudio Smiraglia[2]

Received 18 September 2009; revised 3 December 2009; accepted 10 December 2009; published 7 May 2010.

[1] During the 2005–2007 June–September ablation seasons, meteorological conditions were recorded on the lower and upper parts of the debris-covered ablation zone of Miage Glacier, Italy. In 2005, debris temperature and subdebris ice melt were also monitored at 25 points with debris thickness of 0.04–0.55 m, spread over 5 km^2 of the glacier. The radiative fluxes were directly measured, and near-closure of the surface energy balance is achieved, providing support for the bulk aerodynamic calculation of the turbulent fluxes. Surface-layer meteorology and energy fluxes are dominated by the pattern of incoming solar radiation which heats the debris, driving strong convection. Mean measured subdebris ice melt rates are 6–33 mm d^{-1}, and mean debris thermal conductivity is 0.96 W m^{-1} K^{-1}, displaying a weak positive relationship with debris thickness. Mean seasonal values of the net shortwave, net longwave, and debris heat fluxes show little variation between years, despite contrasting meteorological conditions, while the turbulent latent (evaporative) heat flux was more than twice as large in the wet summer of 2007 compared with 2005. The increase in energy output from the debris surface in response to increasing surface temperature means that subdebris ice melt rates are fairly insensitive to atmospheric temperature variations in contrast to debris-free glaciers. Improved knowledge of spatial patterns of debris thickness distribution and 2 m air temperature, and the controls on evaporation of rainwater from the surface, are needed for distributed physically based melt modeling of debris-covered glaciers.

Citation: Brock, B. W., C. Mihalcea, M. P. Kirkbride, G. Diolaiuti, M. E. J. Cutler, and C. Smiraglia (2010), Meteorology and surface energy fluxes in the 2005–2007 ablation seasons at the Miage debris-covered glacier, Mont Blanc Massif, Italian Alps, *J. Geophys. Res.*, *115*, D09106, doi:10.1029/2009JD013224.

1. Introduction

[2] Debris-covered glaciers, which have a continuous mantle of rock debris over the full width of at least part of their ablation areas, are found in most of the world's major mountain ranges, and are particularly extensive in the high Asian mountain chains, Alaska and central Andes [*Kirkbride*, 2010]. Expansion of supraglacial debris cover concurrent with recent glacier shrinkage has been widely documented [e.g., *Deline*, 2005; *Stokes et al.*, 2007; *Bolch et al.*, 2008]. Glacial meltwater is an increasingly important water resource, particularly in arid-zone mountain regions where debris-covered glaciers are common [*Hewitt et al.*, 1989; *Beniston*, 2003; *Mayer et al.*, 2006; *Viviroli et al.*, 2007]. Thus, studies of the surface energy balance of debris-covered glaciers, which link surface melt rates to climate, are important.

[3] Supraglacial debris cover has a major impact on glacier mass balance through its influence of surface melt [*Popovnin and Rozova*, 2002]. Dispersed and thin debris enhance ice melt rates through albedo reduction, whereas debris mantles of more than a few cm thickness reduce ice melt by insulating it from atmospheric heat and insolation [*Østrem*, 1959; *Adhikary et al.*, 2000; *Kirkbride and Dugmore*, 2003; *Mihalcea et al.*, 2006]. While the surface energy balance of debris-free glaciers has been studied extensively in all climate zones, including the tropics [e.g., *Favier et al.*, 2004; *Mölg and Hardy*, 2004], midlatitudes [e.g., *Greuell and Genthon*, 2004; *Hock*, 2005] and polar regions [e.g., *Van de Wal et al.*, 2005; *Hoffman et al.*, 2008] only a few short-term studies have investigated the energy balance of debris-covered snow and ice [*Nakawo and Young*, 1981, 1982; *Mattson and Gardner*, 1989; *Kayastha et al.*, 2000; *Takeuchi et al.*, 2000; *Adhikary et al.*, 2002; *Nicholson and Benn*, 2006; *Brock et al.*, 2007]. Knowledge of meteorological conditions across debris-covered glaciers is limited to pilot studies [e.g., *Fujita and Sakai*, 2000; *Mihalcea et al.*, 2006] and detailed micrometeorological experiments have been lacking. Determination of the debris

[1]School of Social and Environmental Sciences, University of Dundee, Dundee, UK.
[2]Department of Earth Sciences, University of Milan, Milan, Italy.

0148-0227/10/2009JD013224

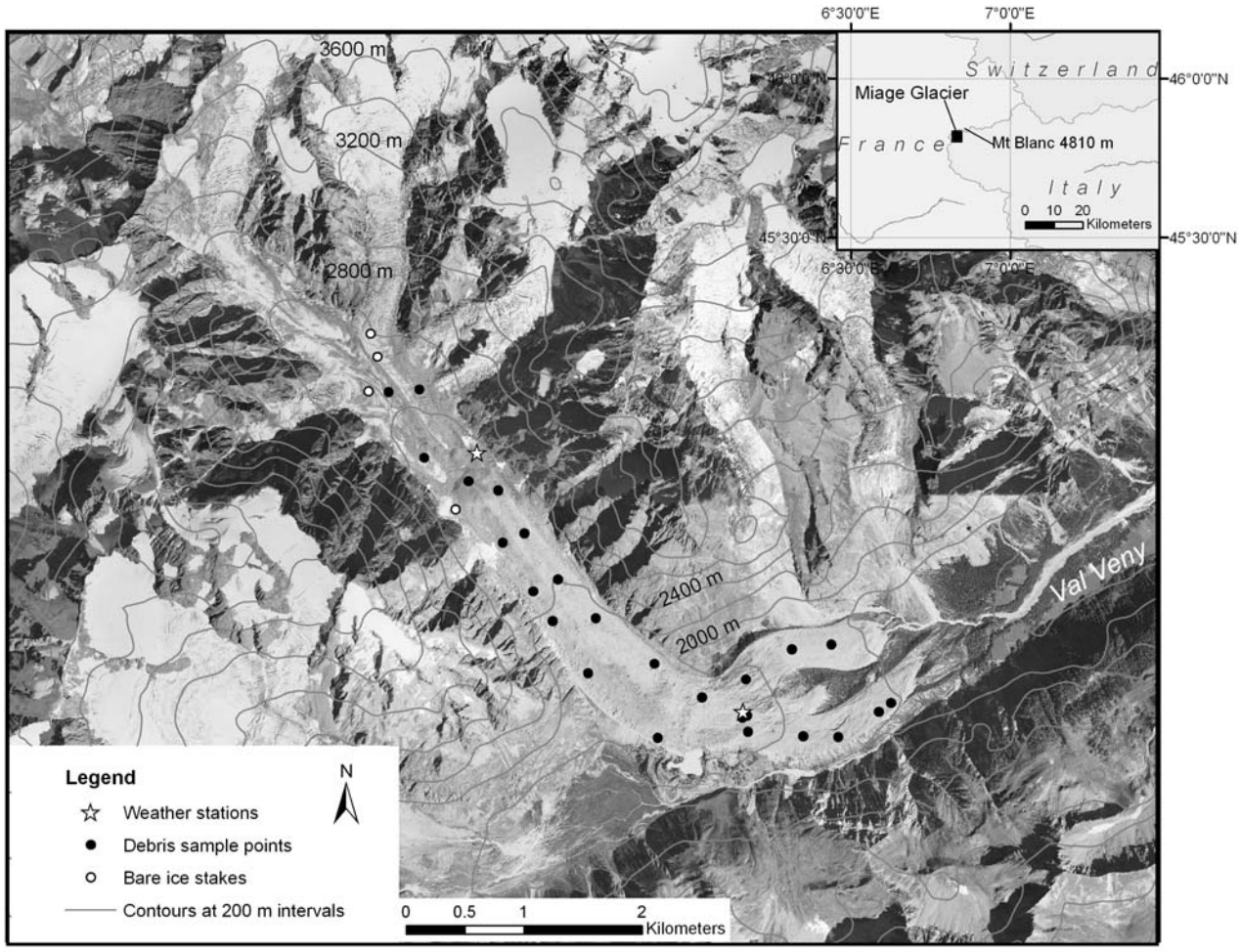

Figure 1. Site map of Miage Glacier showing weather station and sample point locations. The insert shows the location of study area.

thermal properties, temperature and humidity values needed for modeling melt beneath debris covers is problematic, while little is known about the impact of variation in atmospheric stability, and the role of evaporation and condensation in the debris surface energy balance [*Nicholson and Benn*, 2006; *Brock et al.*, 2007]. Empirical degree-day approaches are normally used [e.g., *Mihalcea et al.*, 2006; *Singh et al.*, 2006; *Hagg et al.*, 2008] owing to limited data availability in remote mountain locations and poor knowledge of key processes. Better understanding of the surface energy balance of debris-covered glaciers is needed for management of water resources and calculation of future water yield, including the contribution of mountain glaciers to eustatic sea level change.

[4] The main aims of this paper are: (1) to quantify the energy fluxes at the surface of a supraglacial debris cover using detailed micrometeorological measurements; (2) to record and explain patterns of variation in surface layer meteorology across a debris-covered glacier. These aims are important steps in the development of distributed physically based energy-balance models for debris-covered glaciers and to evaluate their sensitivity to climatic warming. In particular, methods to calculate the turbulent fluxes and to treat variation in atmospheric stability need to be tested; and the response of debris surface temperature, and hence the debris heat flux and subdebris ice melt rate, to different meteorological conditions must be explained.

2. Study Site

[5] Miage Glacier has an area of approximately 11 km^2 and is located on the southwest flank of the Mont Blanc Massif in northwest Italy (45°47′N, 06°52′E) (Figure 1). About 5 km^2 of the ablation zone is debris-mantled owing to high rates of debris supply from surrounding rock walls through frost weathering processes, permafrost degradation, structural rockfalls [*Deline*, 2009] and mixed snow/rock/ice avalanching from accumulation zones (3000–4800 m asl). Recent thinning of the glacier tongue [*Diolaiuti et al.*, 2009] is also likely to be exposing englacial debris. Medial moraines, which form below tributary confluences between 2500 and 2600 m asl, develop into continuous debris cover below 2400 m above sea level (asl), which has a varied lithology dominated by schists and granites on the western and eastern sides of the tongue, respectively. Debris thickness increases from a few centimeters of dispersed cover on the upper tongue to >1 m at the terminus at 1775 m asl, although debris cover is patchy or absent in localized areas

Table 1. Meteorological and Debris Surface Measurements[a]

Year	Weather Station Elevation (m asl)	Variables Measured[b]	Period
2005	lower 2030	$[S\downarrow, S\uparrow, L\downarrow, L\uparrow]_{1.5}$, $[T, U, u]_{0.5,\ 1.0\ \text{and}\ 2.0}$, $[u, w]_{2.5}$, T_s, $T_{d\ -0.03}$, T_{di}, U_s	15/06–08/09
2006	lower 2030	$[S\downarrow, S\uparrow, L\downarrow, L\uparrow]_{1.5}$, $[T, U, u, w]_{2.0}$, T_s, T_{di}	05/06–07/09
	upper 2340	$S\downarrow$, $[T, U, u]_{2.0}$, T_s, $T_{d\ -0.05}$, T_{di}	06/06–06/09
2007	lower 2030	$[S\downarrow, S\uparrow, L\downarrow, L\uparrow]_{1.5}$, $[T, U, u, w]_{2.0}$, T_s, $T_{d\ -0.02}$, T_{di}, U_s	19/06–05/09
	upper 2340	$S\downarrow$, $[T, U, u]_{2.0}$, T_s, T_{di}	22/06–02/09

[a]$L\downarrow$, incoming longwave radiative flux; $L\uparrow$, outgoing longwave radiative flux; $S\downarrow$, $S\uparrow$, incident and reflected (outgoing) shortwave radiative fluxes; T, air temperature; T_s, surface temperature; T_d, debris temperature; T_{di}, temperature at the debris-ice interface, u, wind speed; U, air humidity; U_s, surface humidity; w, wind direction. Subscripts give nominal heights above (below for negative numbers) the surface in meters. T and U were shielded and artificially ventilated in 2005; shielded and naturally ventilated in 2006 and 2007.

[b]Variables were sampled at 1 s intervals and recorded as mean values every 10 min in 2005 and every hour in 2006 and 2007 on Campbell Scientific, Gemini Tinytag, and Onset HOBO data loggers.

of crevasses. Between 2000 and 2400 m asl the surface gradient is shallow, on average 10°, but steepens to 20° below 2000 m asl on the terminal lobes. Post Little Ice Age retreat has been much less than at nearby debris-free glaciers owing to the insulating effect of the debris cover [*Deline*, 2005].

3. Measurement Program

[6] Meteorological measurements were conducted on the debris-covered ablation zone of Miage Glacier at two sites: a lower weather station (LWS) at 2030 m asl representative of the exposed lower ablation area, and an upper weather station (UWS) at 2340 m asl representative of the more topographically confined upper ablation area, close to the upper limit of continuous debris-cover (Figure 1). In 2005 a detailed boundary layer experiment was conducted at the LWS site alone, whereas in 2006 and 2007 energy balance stations were deployed at both the LWS and UWS sites (Table 1). The surface at both sites was level comprising a mixture of granites and schists of predominantly cobble size, with occasional boulders of <1 m size. Debris temperature, thickness and subdebris ice ablation were monitored throughout the 2005 ablation season at 25 sample points representative of the entire debris-covered area (Figure 1). Hourly precipitation totals were recorded at Lex Blanche station, owned by Regione Valle d'Aosta, 4 km west of the LWS at 2162 m asl.

3.1. Radiative Fluxes

[7] Fluxes of incoming and outgoing short and longwave radiation ($S\downarrow$, $S\uparrow$, $L\downarrow$ and $L\uparrow$) were measured at the LWS using a Kipp & Zonen CNR1 sensor (Tables 1 and 2). At the UWS, only $S\downarrow$ was measured using a Skye pyranometer. All radiation sensors were leveled horizontally to record fluxes perpendicular to the surface. Hence, $S\downarrow$, the shortwave irradiance, is equivalent to the global radiation. Longwave radiation measurements were adjusted to account for the influence of solar radiation following the manufacturer's recommendations and experiments with the CNR1 sensor at sites with high levels of incident shortwave radiation [e.g., *Sicart et al.*, 2005]:

$$L\downarrow = L\downarrow_{measured} - 0.02\,S\downarrow \quad (1)$$

3.2. Air Temperature and Humidity Measurements

[8] Air temperature T, and humidity U, sensors were shielded from solar radiation and artificially aspirated during 2005, but in 2006 and 2007 naturally ventilated radiation shields were used owing to the difficulty of supplying power to the weather stations (Tables 1 and 2). Potential errors in the naturally ventilated T measurements were assessed through comparison with simultaneous artificially aspirated T measurements at 2 m height at the LWS during a 44 day period in 2005. Differences between the naturally venti-

Table 2. Sensor Specifications

Quantity	Manufacturer	Type	Accuracy According to the Manufacturer
Air temperature[a], °C	Vaisala	HMP45C	±0.2°C
Relative humidity[a], %	Vaisala	HMP45C	±2% in 0–90% range, ±3% in 90–100% range
Wind speed, m s^{-1}	Vector	A100L	1% ±0.1 m s^{-1}, threshold 0.15 m s^{-1}
Wind direction[b], °	Young	05103	±3°
Incident shortwave radiation, W m^{-2}	Kipp & Zonen[b]	CM3, $0.305 < \lambda < 2.8$ μm[c]	±10% for daily sums
	Skye[d]	SP1110, $0.35 < \lambda < 1.1$ μm	±3%
Reflected shortwave radiation[b], W m^{-2}	Kipp & Zonen	CM3, $0.305 < \lambda < 2.8$ μm	±10% for daily sums
Incoming longwave radiation[b], W m^{-2}	Kipp & Zonen	CG3, $5 < \lambda < 50$ μm	±10% for daily sums
Outgoing longwave radiation[b], W m^{-2}	Kipp & Zonen	CG3, $5 < \lambda < 50$ μm	±10% for daily sums
Debris temperature, °C	Gemini Tinytag	PB-5001, 10K NTC thermistor	±0.2°C in −5° to +65°C range
Debris relative humidity[b], %	Onset	HOBO Temperature/RH Smart Sensor	±4%

[a]At the Lower AWS in 2005 the Vaisala hygrothermometers were shielded from solar radiation and artificially aspirated using RM Young 43408-2 aspirated radiation shields and at other times shielded and naturally ventilated using Campbell URS1 radiation shields.

[b]Lower AWS only.

[c]The spectral range of the radiation sensors is given in wavelength (λ).

[d]Upper AWS only. The Skye pyranometer measurements were cross-calibrated to the upfacing CM3 sensor using 85 days of simultaneous measurement at the LWS in 2005 (12234 10 minute samples, R^2 = 99.8%, mean difference = −0.1 W m^{-2}, RMS difference = 15.6 W m^{-2}).

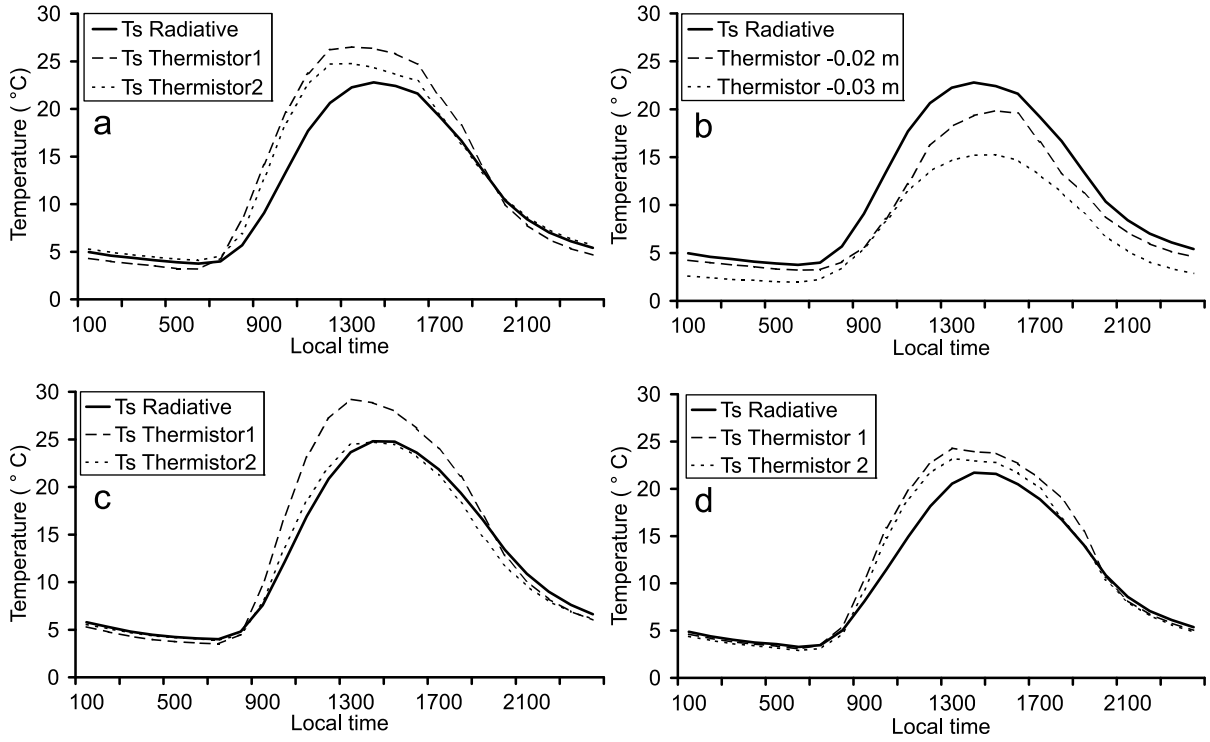

Figure 2. Comparison of radiative (ε = 0.94) and thermistor measurements of debris surface temperature (Ts): mean daily cycles in the (a and b) 2005 season, (c) 2006 season, and (d) 2007 season. Figure 2b shows traces for buried thermistors at depths shown.

lated and artificially aspirated T measurements were small (mean = < 0.01°C, RMS = 0.53°C) and independent of $S\downarrow$. This is in contrast to results of similar experiments above clean glacier surfaces [e.g., *Arck and Scherer*, 2001]. The most likely explanation is that $S\uparrow$, the main cause of overheating of temperature sensors in standard radiation shields [*Georges and Kaser*, 2002], is small above debris owing to the relatively low surface albedo of rock, combined with high wind speed (mean = 3.0 m s^{-1} during daylight hours) when $S\downarrow$ is large. Regression of the difference between naturally ventilated and artificially aspirated T on other meteorological variables resulted in negligible improvement to the mean and RMS difference. Consequently, naturally ventilated T measurements were not altered prior to further analysis.

3.3. Surface Temperature and Humidity

[9] Surface temperature, T_s, was measured at all debris sample points and at the LWS and UWS using negative temperature coefficient K-type thermistors (Table 2). T_s measurement using thermistors can suffer from problems of sensor heating and cooling independently of the surface [*Mihalcea et al.*, 2008a]. To minimize such errors, each thermistor was bound to a clean flat rock ensuring the thermistor tip was in firm contact with the upfacing surface. Direct contact between the thermistor and clast, and the relatively high albedo of the thermistor, should ensure that the thermistor temperature is representative of the rock surface temperature. The spatial representativeness of the 0.01 m^2 scale thermistor measurements was assessed by sampling directly beneath the down-facing CG3 sensor at the LWS, for comparison with the radiatively derived T_s which "samples" several m^2 of debris. Two thermistors in 2005 and 2007, and one in 2006, were installed using the "standard" method described above. In 2005, two additional thermistors were installed below the surface at depths of 0.02 and 0.03 m, and in 2006 a second thermistor was installed in a partly shaded area among rock clasts. Radiative T_s was calculated assuming a surface broadband emissivity of 0.94 on the basis of published values for granitic and metamorphic rocks [*Hartmann*, 1994].

[10] Thermistors installed using the "standard" method overestimate mean daytime radiative T_s by 3–4°C, whereas nighttime thermistor T_s corresponds very closely (within 1°C) with radiative T_s (Figure 2). Daytime overestimation by the thermistors probably occurs because clean upfacing clasts represent the warmest areas of the debris surface, while longwave emission recorded by the CG3 sensor includes a mixture of surfaces of varying aspects, and shaded areas. This interpretation is supported by the partly shaded thermistor in 2006 which almost perfectly matches radiative T_s (Figure 2c). The buried thermistors underestimate radiative T_s by up to 8°C during the daytime and up to 2°C during the nighttime, indicating steep gradients of several °C cm^{-1} in the topmost layer of debris (Figure 2b). This result, and the difficulty of installing and maintaining thermistors at a consistent depth, precludes this method for sampling debris T_s. Consistent sampling is also a problem in the "standard" method. Differences in clast albedo and aspect can result in T_s variability of 1 or 2°C during the middle part of the day (Figures 2a and 2d). Radiative T_s derived from the down-facing CG3 sensor is therefore

Table 3. Mean and Extreme Values of Meteorological Variables at Lower and Upper Weather Stations[a]

Meteorological Variable	2030 m asl			2340 m asl	
	Lower 2005	Lower 2006	Lower 2007	Upper 2006	Upper 2007
2 m temperature mean (°C)	10.7	11.1	10.2	8.7	8.1
2 m temperature maximum (°C)	22.1	23.4	21.5	20.4	18.4
2 m temperature minimum (°C)	0.3	0.2	−0.1	−1.4	−1.5
2 m relative humidity (%)	66	68	69	63	69
2 m vapor pressure (Pa)	831	819	788	688	659
2 m humidity mixing ratio (g kg^{-1})	6.5	6.4	6.1	5.5	5.3
2 m wind speed (m s^{-1})	2.6	2.9	3.1	2.1	2.4
Directional constancy	0.61	0.66	0.68	-	-
Incoming shortwave radiation (W m^{-2})	250	259	256	205	201
Albedo	0.13	0.13	0.15	-	-
Net longwave radiation (W m^{-2})	−70	−75	−72	-	-
Incoming longwave radiation (W m^{-2})	299	297	293	-	-
Outgoing longwave radiation (W m^{-2})	369	373	365	-	-
Surface temperature (thermistor) (°C)	12.9	13.5	11.7	11.1	9.7
Surface temperature (radiative) (°C)	11.3	12.1	10.7	-	-
Surface temperature maximum[b] (°C)	36.5	36.5	31.6	-	-
Surface temperature minimum[b] (°C)	−2.1	−1.8	−1.5	-	-
Surface vapor pressure (Pa)	887	-	889	-	-
Surface humidity mixing ratio (g kg^{-1})	6.9	-	6.9	-	-

[a]During the 22 June to 2 September period, which represents the longest period simultaneous measurements of all variables are available at all stations in each year, enabling direct comparison between different seasons and sites. There are 2036 hourly means. Owing to instrument failure, surface humidity was not recorded in 2006.
[b]Radiative surface temperature.

considered the most reliable method and will be used in all energy flux calculations.

[11] Surface humidity U_s, was measured using a HOBO Smart Sensor (Table 2). The sensor is housed in a perforated aluminum sleeve of 1.5 cm diameter and 10 cm length which was installed level with the debris surface. Instrument failure meant no U_s data were recorded in 2006, but complete records were retrieved in 2005 and 2007.

3.4. Ice Ablation, Debris Thickness, and Thermal Conductivity Measurements

[12] In the 2005 ablation season 25 debris sample points were established, ranging in elevation from 1839 to 2419 m asl over 5 km^2 of debris cover with thickness ranging from 0.04 m to 0.55 m (Figure 1). Subdebris ice melt rates were monitored at each sample point using ablation stakes, made of low-conductivity white plastic tubes of 3 m length. Debris thickness was measured during installation in June and during the monitoring of stakes in July and September. Bare ice melt rates were recorded at two stakes on the western side of the glacier tongue (ice with a covering of dust; mean albedo 0.18) between 11 June and 7 July 2005, and at two stakes at the base of the main tributary glacier ice fall (clean ice; mean albedo 0.34) between 22 June and 26 July 2007 (Figure 1).

[13] T_s (using the "standard" thermistor method; see section 3.3), and the temperature at the base of the debris layer, T_{di}, were monitored at each debris sample point over the same periods as the ablation measurements. Simultaneous measurement of subdebris ablation, debris thickness and temperature gradient normal to the surface enables calculation of debris effective thermal conductivity, K_e, following *Nakawo and Young* [1982] and *Brock et al.* [2007]:

$$K_e = \frac{d.\overline{G}}{\overline{T_s - T_{di}}} \quad (2)$$

where K_e is the effective thermal conductivity (W m^{-1} K^{-1}), d is the thickness of the debris layer (m); $\overline{G}$ is the conductive heat flux through the debris averaged over time, assumed equal to $\overline{M}$, the mean ice melt energy flux beneath the debris (W m^{-2}); and $\overline{T_s - T_{di}}$ is the mean temperature difference between the top and the bottom of the debris layer. T_{di} was within a few tenths of a degree of 0°C throughout the measurement periods at all sites so it could be assumed all heat energy conducted to the debris base was used in melting ice. Owing to the likely overestimation of $\overline{T_s}$ by thermistors (section 3.3), it was reduced by 1.3 K at each site; the mean difference between thermistor and radiative T_s at the lower AWS between 2005 and 2007 (Table 3). $\overline{M}$ was calculated from the ablation stake measurements using the latent heat of fusion of ice at 0°C (0.334 MJ kg^{-1}), divided by time, assuming an ice density of 890 kg m^{-3}. The method assumes that the net change in heat stored in debris over time is negligible and that the mean vertical temperature gradient is linear, which are acceptable assumptions over periods of a week or more [*Conway and Rasmussen*, 2000; *Nicholson and Benn*, 2006]. The derived thermal conductivity value is termed "effective" to acknowledge that heat transfer through debris may not be entirely due to conduction, but may include convection through voids in unconsolidated clast layers, evaporation, condensation and percolation of rainwater. K_e is, however, the most useful quantity for melt modeling.

4. Results: Meteorological Conditions

4.1. Wind Field

[14] The LWS site is dominated by the prevailing synoptic-scale westerly airflow between 200 and 300°, aligned with the long axis of Val Veny (Figures 1 and 3). A secondary mode around 70° is associated with NE winds blowing up Val Veny. Wind speed, u, is low (mean = 0.8–1.6 m s^{-1}) for N and E directions between 320° and 180° but peaks at

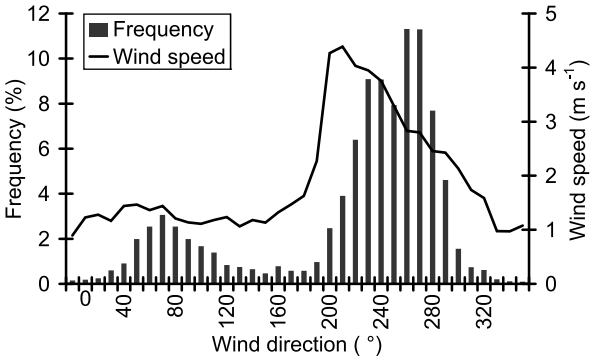

Figure 3. Mean hourly 2 m wind speed and frequency against wind direction, LWS site, 2005–2007 seasons (5985 measurements).

>4 m s^{-1} for SW winds between 200° and 220°. Wind direction and speed follow clear daily patterns (Figure 4). Wind direction backs from WSW to SSE between 900 and 1200, as a valley wind, driven by convection above the warming debris cover, becomes established. Prior to the arrival of the valley wind, *u* decreases to <2 m s^{-1} at 1000 h, subsequently increasing to >4 m s^{-1} at 1700 as wind direction gradually veers to WSW. At the UWS *u* follows a similar daily cycle, but with lower magnitude (Table 3 and Figure 4), reflecting weaker convective heating and the shelter provided by the deep trough of the main valley tongue aligned orthogonally to prevailing synoptic-scale winds.

[15] Directional constancy, defined as the ratio of the magnitude of the time-averaged wind vector and time-averaged wind speed, is high and similar in each year at the LWS (Table 3), but lower than the values >0.80 reported on the tongue of the similarly sized debris-free Pasterze Glacier, where strong katabatic winds dominate [*Greuell et al.*, 1997]. Mean *u* at the LWS is between 2.6 and 3.1 m s^{-1} (Table 3), similar to values for Haut Glacier d'Arolla, a smaller debris-free valley glacier in Switzerland [*Strasser et al.*, 2004], but around 1 m s^{-1} lower than values on Pasterze Glacier [*Greuell et al.*, 1997]. Mean *u* was 0.6 m s^{-1} lower at the UWS.

4.2. Temperature

[16] Mean seasonal 2 m *T* at the LWS ranged from 10.2°C in 2007 to 11.1°C in 2006 (Table 3). 2005 and 2006 were very warm summers in central Europe whereas 2007 was close to the 1961–1990 mean (http://hadobs.metoffice.com/crutem3; *Brohan et al*. [2006]). During fine weather, daytime *T* normally exceeds 18°C, with an absolute maximum of 23.4°C recorded in 2006 (Table 3). No air frosts were recorded in 2005 or 2006 at the LWS and only two slight air frosts (−0.1°C) occurred in 2007. Ground frosts were more common, occurring on average once every 5 nights in 2007 and once every 14 nights in 2006. Mean seasonal *T* was over two degrees cooler at the UWS (Table 3), with seven air frosts recorded in both the 2006 and 2007 summers, and extreme values of −1.5°C and 20.4°C, respectively. Ground frosts were about twice as frequent at the UWS as at the LWS.

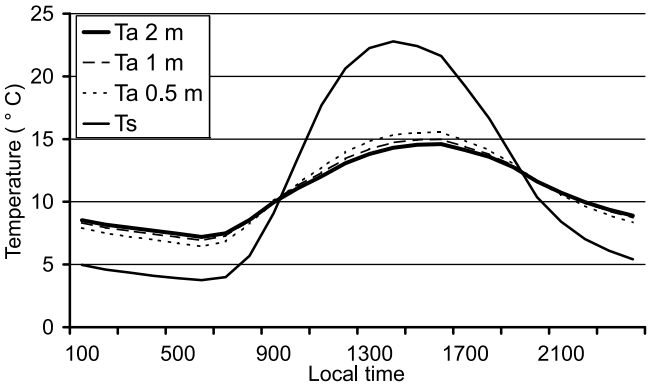

Figure 5. Mean daily cycles of hourly radiative surface temperature (Ts) and mean air temperature (Ta) at three heights (0.5, 1.0, and 2.0 m); lower AWS site, 2005 season.

[17] The daily cycle of *T* shows a strong relationship to T_s, being driven by convective and radiative heating from the debris during the daytime and cooling by sensible heat transfer at nighttime (Figure 5). The mean daily cycle of T_s has a much larger amplitude than *T*, with nighttime minima and daytime maxima of 4° and 23°C, respectively, but peaking >30°C on sunny days. A temperature inversion is usually present between 2000 and 0900 h in the 2 m surface layer, while 0.5 m *T* is on average over a degree warmer than 2.0 m *T* during the afternoon (Figure 5). Changes in vertical temperature structure in the 2 m surface layer during

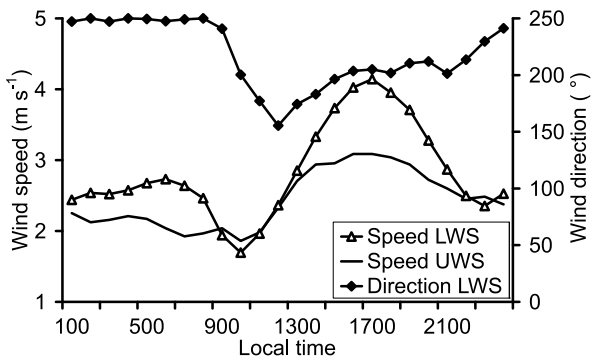

Figure 4. Mean daily cycles of hourly wind speed at the LWS and UWS (principal axis) and wind direction at the LWS (secondary axis); the example is of the 2007 season.

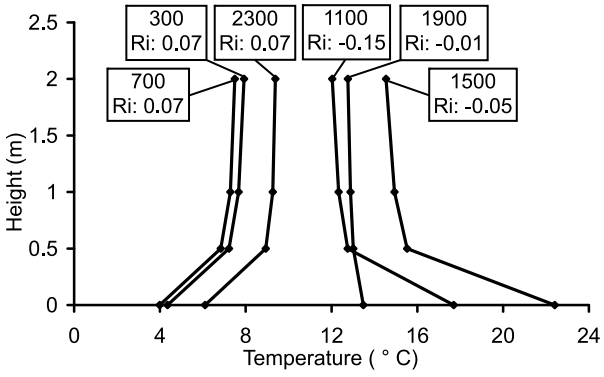

Figure 6. Mean vertical temperature profiles and corresponding gradient Richardson numbers Ri, at 0300, 0700, 1100, 1500, 1900 and 2300 LT; lower AWS site, 2005 season.

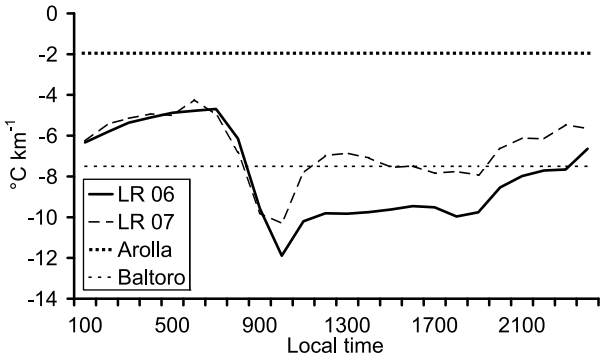

Figure 7. Mean daily cycles of the hourly temperature lapse rate between the LWS and UWS, 2006 and 2007 seasons (LR 06 and LR 07), and published mean temperature lapse rates for debris-free ("Arolla," data for Haut Glacier d'Arolla, Switzerland; see *Strasser et al.* [2004]) and debris-covered ("Baltoro," data for Baltoro Glacier, Pakistan; see *Mihalcea et al*. [2006]) glaciers.

the course of a typical day at the LWS are illustrated in Figure 6. Nighttime profiles are characterized by stable stratification, with similar Richardson Number values to those reported for debris-free glaciers [*Sicart et al.*, 2005]. With surface heating during the morning, the surface layer becomes unstable owing to the combination of low u (Figure 4) and steep vertical temperature gradient. The midmorning is therefore characterized by weak horizontal motion and strong convective instability transferring heat from the debris to the atmosphere. The surface layer remains unstable until the late afternoon, but instability is reduced by increasing u. With decreasing T_s, neutral conditions occur briefly in the early evening, before the transition back to stable stratification overnight.

[18] The mean 2 m temperature lapse rate between the LWS and the UWS ranged from −8.0°C km^{-1} in 2006 to −6.7°C km^{-1} in 2007, similar to the mean of −7.5°C km^{-1} at debris-covered Baltoro Glacier, Pakistan [*Mihalcea et al.*, 2006]. There is a clear daily cycle in mean temperature lapse rate (Figure 7). The rapid steepening between 700 and 1000 occurs because the lower glacier is exposed to solar heating from dawn, while the upper ablation area is in shade until after 900 (Figures 1 and 8). During the remainder of the day the lapse rate gradually declines, but remains steeper than a "standard" atmosphere reflecting warmer daytime conditions on the lower glacier. During the nighttime the air temperature environment is dominated by surface cooling, as on a debris-free glacier, but the mean lapse rate is always higher than the mean of −2°C km^{-1} reported for Haut Glacier d'Arolla [*Strasser et al.*, 2004]. The temperature lapse rate was shallower in the cooler and cloudier 2007 summer (Figure 7).

4.3. Humidity

[19] Two m vapor pressure and humidity mixing ratio were similar in 2005 and 2006, but lower in the cooler 2007 summer (Table 3). On average, the humidity mixing ratio was 0.8 to 0.9 g kg^{-1} lower at the UWS than the LWS. Mean surface vapor pressure and surface humidity mixing ratio were higher than their respective 2 m values, indicating that moisture gradients were directed away from the surface more often than toward it (Table 3). Mean surface humidity in 2007 was almost identical to 2005, despite the lower T_s, owing to more frequent rainfall. As a consequence, surface layer moisture gradients were steeper in 2007 than 2005.

4.4. Shortwave Radiation

[20] Interannual variations in mean $S\downarrow$ were small, but mean annual values were >50 W m^{-2} (about 20%) lower at the UWS (Table 3) owing to greater topographic shading, particularly before 1000 h, and build up of cumulus clouds over the Mont Blanc Massif during the afternoon (Figure 8). Albedo was low and consistent between years at the LWS (Table 3). The higher mean albedo in 2007 was due to a snowfall in early July, when a maximum value of 0.70 was reached. Albedo minima of 0.06 occurred when the surface was wet. Point sampling in different areas of debris using a portable albedometer (model Kipp & Zonen CM7B) revealed little spatial variation in albedo, ranging from 0.12 to 0.16 between areas of schist and granite and quartz-rich rocks, respectively. In most areas, the surface lithology is a mixture of rock types and hence debris albedo is probably of minor importance to spatial variations of the net shortwave radiation flux.

[21] $S\downarrow$ is affected by several processes between the top of the atmosphere and the glacier surface: absorption and scattering by aerosols, clouds and gases in the atmosphere; multiple reflections between the atmosphere and the ground and horizon obstruction and reflections from surrounding topography. The clear-sky direct incoming shortwave radiation arriving at a horizontal surface, S_0, can be calculated from the product of individual transmittances [e.g., *Strasser et al.*, 2004]:

$$S_0 = 1367 \,.\, \cos(\theta_z) \,.\, \left(\tau_r \,.\, \tau_0 \,.\, \tau_g \,.\, \tau_w \,.\, \tau_a + \beta(z)\right) \qquad (3)$$

where τ_r is transmittance due to Rayleigh scattering, τ_0 the transmittance by ozone, τ_g the transmittance by uniformly mixed trace gases, τ_w the transmittance by water vapor and τ_a the aerosol transmittance. 1367 W m^{-2} is the flux at the top of the atmosphere on a surface normal to the incident radiation, or "solar constant," and θ_z the solar zenith angle.

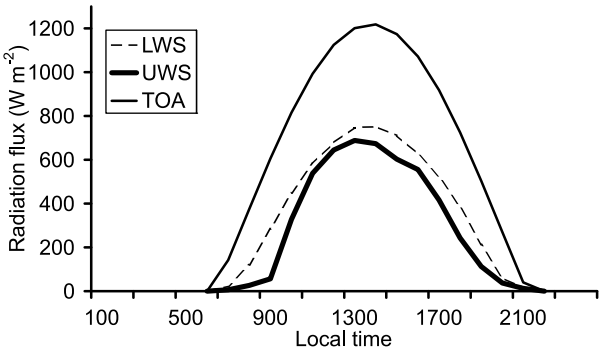

Figure 8. Mean daily cycles of hourly global radiation at the lower and upper automatic weather stations (2006–2007 seasons) and top of atmosphere solar radiation flux (TOA) over the same period for location of Miage Glacier.

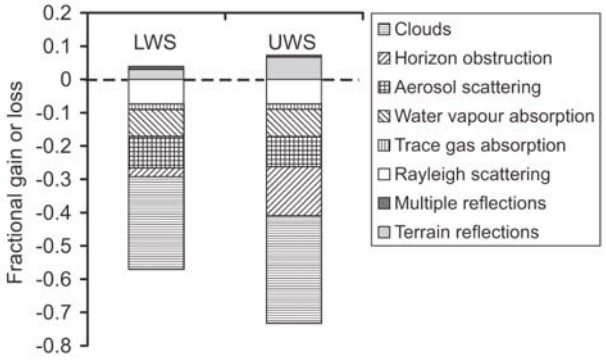

Figure 9. Gain or loss of energy due to different processes affecting the shortwave radiation flux, scaled by the extraterrestrial flux, in the 22 June to 2 September period at the lower weather station (LWS; 2006–2007 seasons) and upper weather station (UWS; 2006–2007 seasons).

$\beta(z)$ accounts for the increase in transmittance with altitude, which is linear up to 3000 m asl [after *Bintanja*, 1996]:

$$\beta(z) = 2.2.10^{-2} \cdot \mathrm{km}^{-1}. \quad (4)$$

Equation 3 was evaluated for both the LWS and UWS, together with the effects of multiple and terrain reflections and horizon obstruction, for the period 22 June to 2 September 2006 and 22 June to 2 September 2007, using a digital elevation model (DEM) of the glacier and surrounding mountains (Advanced Spaceborne Thermal Emission and Reflection Radiometer, ASTER, product with spatial resolution of 30 m and expected vertical accuracy of 30 m, *Bolch et al.*, 2008), T and U measurements and mean air pressure at each weather station, following *Greuell et al.* [1997] and *Strasser et al.* [2004]. Diffuse radiation from a clear sky due to Rayleigh and aerosol scattering, was computed following the method of *Strasser et al.* [2004]. Although this approach is empirically based, calculations closely match observations at mountain sites under clear sky conditions [e.g., *Pellicciotti et al.*, 2005]. The sky view factor (the ratio of the projected surface of visible sky onto the projected surface of a sphere of unit radius) and periods of topographic shading at each site were derived from analysis of the DEM in the geographical information system software package *ArcGIS*. The ground view factor was estimated as (1–sky view factor), an approximation that is valid for flat locations, as at the weather station sites, but not for inclined surfaces [e.g., *Dozier and Frew*, 1990]. In order to determine multiple and terrain reflected radiation, the ground albedo within the field of view of each AWS was defined to be a mixture of bare rock, with an albedo of 0.13, and snow or ice, with an assumed mean albedo of 0.70. The percentage of snow and ice was estimated as 10% for the LWS and 20% for the UWS. Finally, the impact of clouds was evaluated as the ratio of the total measured shortwave radiation to the total calculated clear sky radiation at each AWS.

[22] Figure 9 displays the mean effect of each evaluated process on the extraterrestrial solar flux. The effects of Rayleigh scattering, trace gas, ozone and water vapor absorption and aerosol scattering attenuate the extraterrestrial flux by, on average, 27% at the LWS and 26% at the UWS. Multiple reflections between the sky and ground make a minor contribution to incident energy, while terrain-reflected radiation increases the incoming shortwave flux by almost 7% at the UWS, more than twice as much as at the LWS. The most noticeable difference is in horizon obstruction, which is a minor factor at the more open LWS, reducing the incoming flux by just 3%, but a major factor at the UWS, reducing the incoming shortwave flux by nearly 15%. Clouds had the biggest impact, attenuating the incoming shortwave radiation flux by 28% and 32% at the LWS and UWS, respectively. Topography and cloud cover are clearly important in reducing surface shortwave energy received in the deep trough of the main glacier tongue above 2100 m asl (Figure 1). On average, only 44% of the extraterrestrial shortwave radiation flux reaches the glacier surface at the UWS, while the equivalent value at the LWS is 54%.

4.5. Longwave Radiation

[23] Interannual differences in mean L at the LWS were small (Table 3). L was least negative in the cloudiest year, 2005, while high surface temperatures and outgoing longwave flux were responsible for the largest negative net flux in 2006 (Table 3 and Figure 10). Interannual differences in L were small between midnight and 11 A.M., while large differences occurred between midmorning and late afternoon (Figure 10). Variability in L is most strongly related to daytime debris surface temperature and will thus vary spatially across-glacier as a result of spatial variations in $S\downarrow$ and debris thickness.

5. Results: Ablation Rates and Debris Thermal Conductivity

[24] Measured mean ice melt rate decreases exponentially as a function of d, from 33 mm water equivalent (w.e.) d^{-1} beneath 0.04 m of debris to 6 mm w.e. d^{-1} beneath 0.55 m of debris (Figure 11, equation; significant at $\alpha < 0.001$). Melt rates reported for equivalent debris thicknesses in the Himalaya-Karakorum tend to be slightly higher [*Mattson and Gardner*, 1989; *Kayastha et al.*, 2000; *Mihalcea et al.*, 2006; *Hagg et al.*, 2008], probably because the Miage

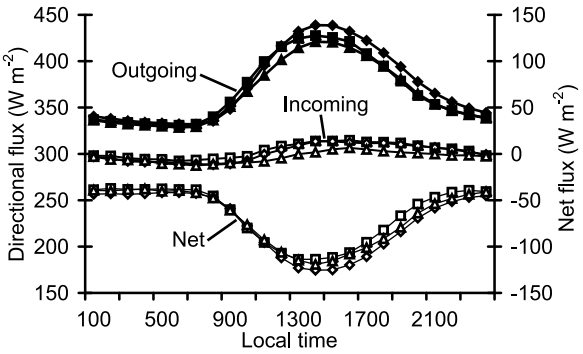

Figure 10. Mean daily cycles of the longwave radiation fluxes at the lower weather station, in the 2005 (squares), 2006 (diamonds), and 2007 (triangles) seasons. Incoming longwave radiation (bold lines and open symbols) and outgoing longwave radiation (bold lines and filled symbols) are on the principal axis; net longwave radiation (thin lines and open symbols) is on the secondary axis.

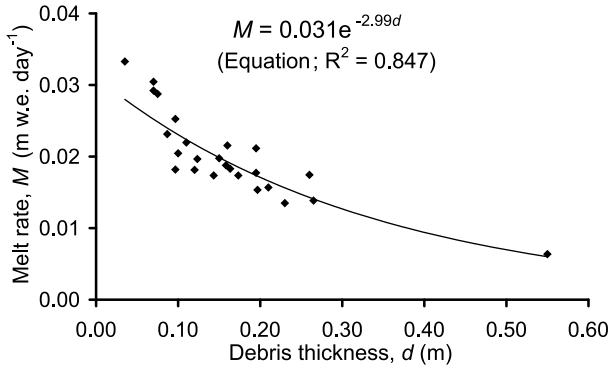

Figure 11. Relationship of mean daily ice ablation, M, to debris thickness, d, at 25 debris sample points in the 2005 season.

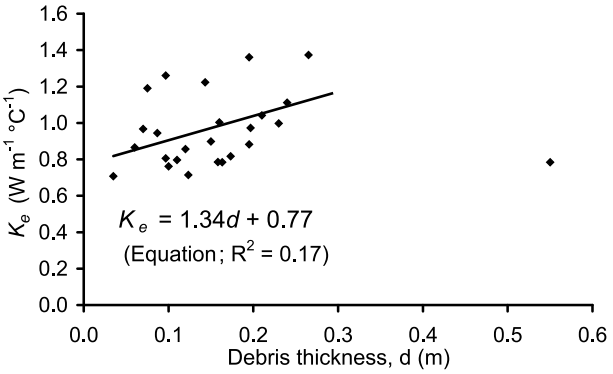

Figure 13. Relationship of effective thermal conductivity, K_e, to debris thickness, d, at 25 debris sample points in the 2005 season.

Glacier measurements include a range of meteorological conditions in a full ablation season at a higher-latitude site. The scatter in melt rate values about the best fit line is attributable to differences in elevation and local topography, considering the sample points cover an elevation range of 580 m and a variety of slope aspects. The relatively high melt rates beneath very shallow debris ($d < 0.09$ m) may be due to incomplete debris cover in the vicinity of these sample points. There is a trend of increasing variability in melt rates up-glacier owing to greater spatial variability in debris thickness between medial moraines and intermoraine areas (Figure 12). The highest melt rates occurred close to the upper limit of the debris cover at around 2400 m asl.

[25] Calculated K_e values range from 0.71 to 1.37 W m^{-1} K^{-1} with a mean of 0.96 W m^{-1} K^{-1}. K_e is weakly, but significantly, dependent on d for covers less than 0.3 m thick (Figure 13, equation; $\alpha < 0.05$). This could be due to greater heat transfer by convection in the larger openwork clast layer normally present in thicker covers. The low K_e at the thickest site ($d = 0.55$ m) close to the glacier terminus is probably due to a layer of soil at the base of the debris. The values are at the lower end of the range quoted for previous direct K_e measurements on debris-covered glaciers (0.85 to 2.6 W m^{-1} K^{-1}; see *Nakawo and Young* [1982] and *Conway and Rasmussen* [2000]) and within the range of 0.47 to 1.97 W m^{-1} K^{-1} estimated from physical constants for typical debris forming materials [*Nicholson and Benn*, 2006].

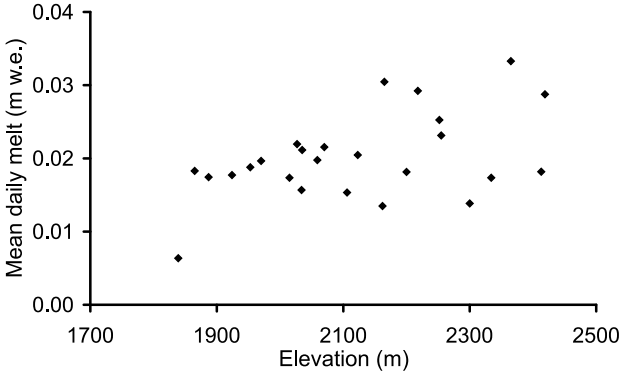

Figure 12. Relationship of mean daily ice ablation to elevation at 25 debris sample points in the 2005 season.

[26] Mean bare (uncovered) ice melt rates ranged from 58 mm w.e. d^{-1} in 2005 to 46 mm w.e. d^{-1} in 2007; two to three times greater than the mean subdebris melt rate of 20 mm w.e. d^{-1} on debris-covered areas and much higher than the maximum measured subdebris melt rate of 33 mm w.e. d^{-1} for the shallowest monitored debris site ($d = 0.04$ m). This implies that the critical debris thickness, at which the subdebris ablation rate equals the bare ice melt rate, is much thinner than 0.04 m. This result contrasts with most earlier studies which identified larger critical debris thicknesses in the 0.03 to 0.09 m range [*Mattson and Gardner*, 1989; *Rana et al.*, 1997; *Kayastha et al.*, 2000]. *Mihalcea et al.* [2006], however, identified that as little as 0.01 m of debris cover reduced the melt rate below the bare ice rate at Baltoro Glacier, Pakistan, again implying a very shallow critical debris thickness. These contrasting results could be partly explained by the fact that d may have been estimated for mixed areas of debris and bare ice some in previous work, whereas we measured d only on continuous debris cover; as well as differences in the lithology of debris-forming materials.

6. Results: Surface Energy Fluxes

[27] The energy balance at the debris surface is expressed as follows (fluxes are in units of W m^{-2} and considered positive when directed toward the surface):

$$S + L + H + LE + P + G + \Delta D = 0 \quad (5)$$

where S and L are the net shortwave and longwave radiation fluxes, respectively, H is the turbulent sensible heat flux, LE is the turbulent latent heat flux (owing to evaporation, condensation or sublimation at the debris surface), P is sensible heat energy supplied or consumed by precipitation falling on the surface, G is the heat flux in the debris and ΔD is the rate of change of heat energy stored in the debris. P is normally ignored in glacier energy balance studies as it is negligibly small compared with the other fluxes. Hence, P was not calculated. ΔD is only considered over periods of a few days or less; over longer periods net ΔD is effectively zero during the ablation season [*Brock et al.*, 2007]. Compared to a clean glacier, the energy balance of a debris-covered ice surface is complicated by highly variable surface temperature, humidity and thermal properties of the surface

material. Direct measurements of these quantities, described in sections 3.1 to 3.4 are used to derive energy flux values.

6.1. Radiative Fluxes

[28] $S\downarrow$, $S\uparrow$, $L\downarrow$ and $L\uparrow$ were measured directly at the lower AWS site (Table 1). Owing to regular leveling of the sensors, low humidity and above-freezing air temperatures, it is assumed that the resulting hourly S and L series represent accurate and reliable records (Table 2).

6.2. Conductive Heat Flux

[29] G was evaluated from the Fourier heat conduction equation:

$$G = K(T_s - T_{di})/d \tag{6}$$

where K is the thermal conductivity, assumed equal to K_e. The mean d at the LWS site was 0.2 m, and a corresponding K_e value of 0.94 (Figure 11, equation) was applied to generate hourly G values for all 3 seasons, using measured T_s and T_{di} values.

6.3. Flux Due to Change in Heat Store in Debris

[30] In order to balance surface energy fluxes at subdaily time intervals, the debris layer must be treated as a volume with variable heat storage:

$$\Delta D = \rho_d C_d \frac{\partial \overline{T}_d}{\partial t} d \tag{7}$$

where ρ_d and C_d are the debris density (kg m^{-3}) and specific heat (J kg^{-1} K^{-1}), respectively, and $\frac{\partial \overline{T}_d}{\partial t}$ is the average rate of temperature change (K s^{-1}) where $\overline{T}_d$ is the mean temperature of the debris layer, calculated as the mean of T_s and T_{di}. At the LWS site the debris consisted of pebble-sized granite and schist clasts with 40% pore spaces, overlying 0.04 m fine grained material which was partially saturated with water. Using published values of density and specific heat [*Robinson and Coruh*, 1988; *Lide*, 2004], values of ρ_d = 1496 kg m^{-3} and C_d = 948 J kg^{-1} K^{-1} were input to equation (7), to calculate ΔD at an hourly interval.

6.4. Turbulent Fluxes

[31] The turbulent fluxes were calculated using the bulk aerodynamic method [*Munro*, 1989; *Denby and Greuell*, 2000; *Arck and Scherer*, 2001]. Previous estimates of turbulent sensible and latent heat fluxes above supraglacial debris have assumed neutral stability [*Nakawo and Young*, 1981, 1982; *Mattson and Gardner*, 1989; *Kayastha et al.*, 2000; *Takeuchi et al.*, 2000; *Adhikary et al.*, 2002; *Nicholson and Benn*, 2006]. This assumption is unlikely to be met given the large variations in atmospheric stability observed in the surface layer (Figure 6) and corrections for nonneutral conditions must be applied. The stability of the surface layer can be described by the bulk Richardson number, Ri_b, which relates the relative effects of buoyancy to mechanical forces [*Brutsaert*, 1982; *Moore*, 1983]:

$$Ri_b = \frac{g(T - T_s)(z - z_{0m})}{T_0 u^2} \tag{8}$$

where g is gravitational acceleration (9.81 m s^{-2}); T_0 is the mean absolute air temperature between the surface and the 2 m measurement level z; and z_{0m} is the surface roughness length for momentum (m), defined as the height above the surface where, assuming a semilogarithmic profile, horizontal wind speed is zero. Stability corrections based on Ri_b have been applied successfully over clean glaciers [e.g., *Favier et al.*, 2004; *Sicart et al.*, 2005] and debris-covered ice [*Brock et al.*, 2007].

[32] z_{0m} was estimated from the wind profile at the lower AWS in 2005, using measurements at the 2.0 and 0.5 m levels, following the method described by *Brock et al*. [2006]. The raw ten minute mean profiles recorded were assembled into half hour averages and only used to calculate z_{0m} if the following criteria were met: (1) u at 2.0 m > u at 0.5 m and maximum wind speed height > 2.0 m (assumed when u at the 2.5 m wind monitor > u at 2.0 m); (2) nonobstructed airflow over a fairly level fetch of at least 500 m, achieved by airflows from a westerly direction; (3) u at 2.0 m > 4 m s^{-1}, to ensure well mixed turbulent flow conditions; (4) near-neutral conditions, defined here by $-0.03 > Ri_b < 0.03$.

[33] The 113 half hour profiles, in the wind direction range 240°–300°, met the above criteria and a single $\ln(z_{0m})$ value was generated from each, giving a mean z_0 value of 0.016 m (95% confidence interval 0.015–0.017 m). The z_0 values are independent of stability, u, wind direction and time. These results correspond with visual observations at the site, where the upwind fetch was dominated by cobble-sized roughness elements with vertical extent at the 0.01 to 0.1 m scale, with no obvious evolution to the size or geometry of surface elements over the measurement period.

[34] Assuming that the local gradients of mean u, mean T and mean specific humidity q are equal to the finite differences between the 2 m measurement level and the surface, the turbulent fluxes may be evaluated as follows [*Brutsaert*, 1982; *Favier et al.*, 2004; *Sicart et al.*, 2005]:

$$H = \rho_a \frac{C_P k^2 u(T - T_s)}{\left(\ln \frac{z}{z_{0m}}\right)\left(\ln \frac{z}{z_{0t}}\right)} (\Phi_m \Phi_h)^{-1} \tag{9}$$

$$LE = \rho_a \frac{L_v k^2 u(q - q_s)}{\left(\ln \frac{z}{z_{0m}}\right)\left(\ln \frac{z}{z_{0q}}\right)} (\Phi_m \Phi_v)^{-1} \tag{10}$$

where q and q_s are specific humidities (kg kg^{-1}) at the 2 m and surface levels, respectively; ρ_a is the air density; C_p is the specific heat capacity for air at constant pressure ($C_p = C_{pd}(1 + 0.84q)$ with C_{pd} = 1005 J kg^{-1} K^{-1}); k is von Karman's constant (k = 0.4) and L_v is the latent heat of vaporization (L_v = 2.476 10^6 J kg^{-1} at 283 K). The scalar lengths for heat z_{0t} and humidity z_{0q} were considered equal to z_{0m}.

[35] The nondimensional stability functions for momentum (Φ_m), heat (Φ_h) and moisture (Φ_v) are expressed as functions of Ri_b [*Brutsaert*, 1982; *Oke*, 1987]:

Stable case, Ri_b positive:

$$(\Phi_m \Phi_h)^{-1} = (\Phi_m \Phi_v)^{-1} = (1 - 5R_{ib})^2 \tag{11}$$

Unstable case, Ri_b negative:

$$(\Phi_m \Phi_h)^{-1} = (\Phi_m \Phi_v)^{-1} = (1 - 16R_{ib})^{0.75}. \tag{12}$$

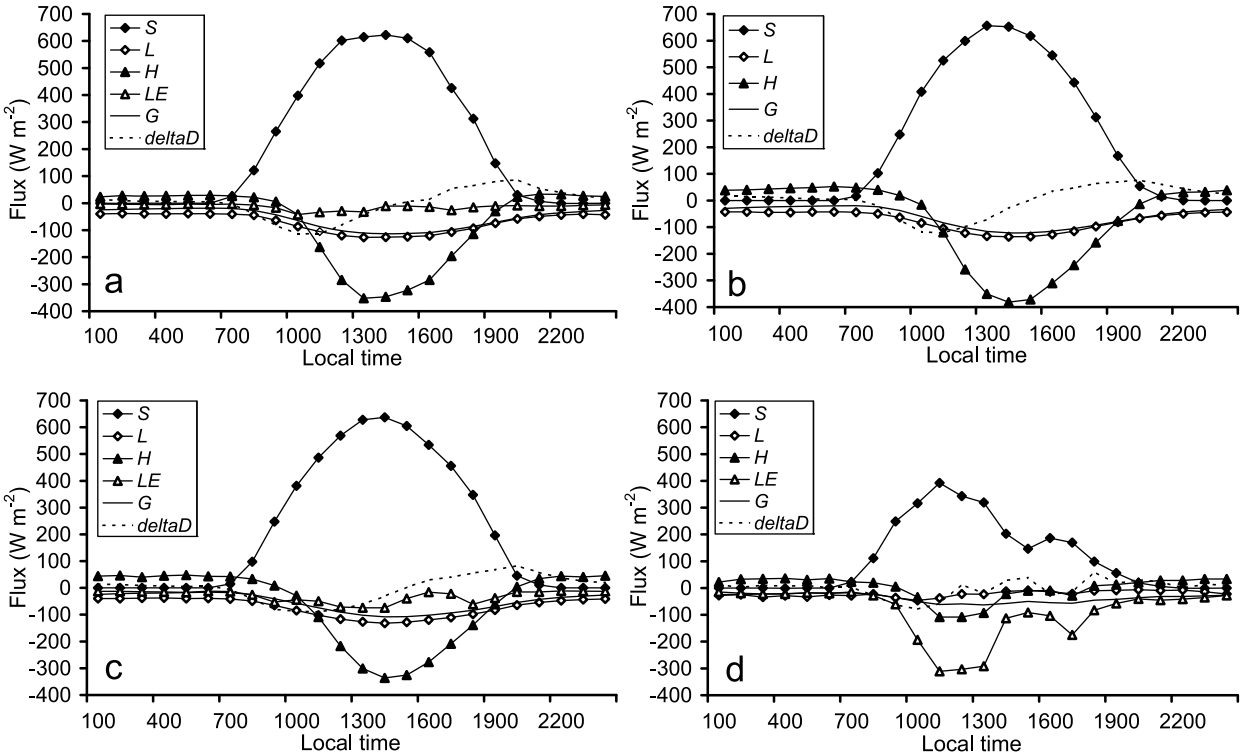

Figure 14. Mean daily cycles of hourly surface energy fluxes at the lower AWS site in the (a) 2005, (b) 2006, and (c) 2007 ablation seasons (the 22 June to 2 September period). (d) Mean daily cycle of hourly surface energy fluxes at the lower AWS site under saturated surface conditions (U_d = 100%) in the 2005 season (356 h, or 20.3% of total observations).

[36] The turbulent fluxes were calculated using mean hourly quantities of all input variables applying: (1) the stability correction on the basis of Ri_b, referred to as $H(Ri_b)$ and $LE(Ri_b)$ hereafter, and, for comparative purposes, (2) assuming neutral atmospheric conditions, referred to as $H(ntl)$ and $LE(ntl)$ hereafter.

6.5. Surface Energy Balance at the Lower Weather Station During the 2005–2007 Ablation Seasons

[37] Mean seasonal values and mean daily cycles of the debris surface energy fluxes at the LWS in the 22 June to 2 September period in each year are shown in Table 4 and Figure 14. The residual energy flux for the complete energy balances in 2005 and 2007 using $H(Ri_b)$ and $LE(Ri_b)$ is close to zero, lending confidence to the calculations and the Ri_b-based stability correction of the turbulent fluxes. In contrast, the assumption of neutral atmospheric conditions generates a large positive residual due to underestimation of the turbulent fluxes $H(ntl)$ and $LE(ntl)$ (Table 4 and Figure 15).

[38] The mean daily cycle of surface energy fluxes is dominated by S and the energy outputs of L, G, and H mirror daytime S values, reflecting the daily cycle of T_s

Table 4. Mean Surface Fluxes (W m^{-2}) at the Lower AWS[a]

Year	S	L	G	H (R_{ib})	H (ntl)	LE (R_{ib})	LE (ntl)	Residual (R_{ib})	Residual (ntl)
2005	219	−70	−57	−75	−21	−14	−11	3	60
2006	225	−75	−60	−76	−25	-	-	14[b]	65[b]
2007	218	−72	−53	−62	−23	−31	−29	0	41

[a]During the 22 June to 2 September period. H and LE values calculated using both the "bulk" Richardson stability correction (R_{ib}), and neutral stability (ntl) methods. S, net shortwave radiation flux; L, net longwave radiation flux; G, debris heat flux; H, sensible heat flux; LE, latent heat flux. Fluxes are positive when directed toward the debris surface.

[b]Residual values in 2006 do not include latent heat flux due to instrument failure.

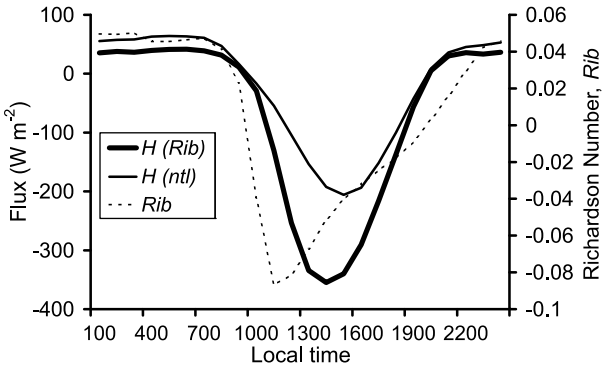

Figure 15. Mean daily cycles of hourly sensible heat flux, 2005–2007 ablation seasons, calculated using bulk Richardson stability correction ($H(Rib)$) and neutral stability ($H(ntl)$) methods (principal axis), and bulk Richardson number (Rib; secondary axis).

Table 5. Precipitation and Evaporation Values During the 22 June to 2 September Period in Each Year

Year	Total Precipitation[a] (mm)	Hours With Rain[b]	Total Evaporation[c] (mm)
2005	274	9.4	36 (13)
2006	386	11.0	–
2007	500	14.4	79 (16)

[a]Lex Blanche weather station.
[b]Shown as percent of total.
[c]Miage lower weather station site. Numbers in parentheses represent percent of total precipitation.

(Table 4 and Figures 14a–14c). ΔD peaks midmorning at > -100 W m^{-2} during the period of most rapid warming of the debris layer, but reverses sign after 1400 as the debris layer begins to cool, and it remains a small positive flux until dawn. Averaged over a season, *LE* is a small negative (evaporative) flux, peaking in midmorning and late afternoon. *LE* is, however, intermittent, ranging from effectively zero under dry conditions to instantaneous values up to 800 W m^{-2} under strong solar heating following rainfall, or when rain falls on hot debris, quickly removing available surface water. Surface energy inputs through condensation on cold nights were negligibly small. During the nighttime, *S* is absent and *H* is a small net energy input to the surface. In contrast, nocturnal *L* and *G* fluxes remain directed away from the surface, albeit of lower magnitude than during the daytime. The nighttime sign reversal of the *H* flux explains why, despite larger daytime values, the mean seasonal flux value is similar to *L* (Table 4).

[39] There is a marked contrast in the mean daily cycle of surface energy fluxes under saturated surface conditions (Figure 14d). *S* is smaller, with low afternoon values associated with cumulonimbus cloud development. The daytime *L* and *G* fluxes are also much smaller, but remain negative. *H* is subdued with daytime values only around a quarter of their seasonal average values. Energy outputs are instead dominated by *LE* which peaks during late morning at >300 W m^{-2}, with a secondary peak in the late afternoon. The high *LE* values correspond with times of strongest solar heating of the surface (Figure 14d) and occur after overnight rain or afternoon showers have fallen. While evaporative *LE* is limited by the presence of surface water, *S* controls the magnitude of this flux.

[40] *G*, *L* and *H* were all largest in the warmest and sunniest year, 2006 (Table 4) when debris surface temperatures were highest (Table 3). Correspondingly, these fluxes were smaller in the coolest and least sunny year of 2007, although *L* was smallest in 2005 owing to the relatively large amount of cloud cover and high air temperature in that year. Overall, *S* and *L*, and to an extent, *G*, show remarkably little variation between years, despite contrasting meteorological conditions. The mean daily ice melt rates from energy supplied by *G* (Table 4) are in the range 14–16 mm w.e. This implies that ablation rates beneath debris are fairly insensitive to variation in mean air temperature between years.

[41] Most of the interannual variability in the debris surface energy balance is associated with the turbulent fluxes. While similar in both 2005 and 2006, *H* was considerably lower in 2007 (Table 4; Figures 14a–14c). This was due to lower surface temperatures, and more frequent periods when *H* was directed toward the surface. The large *LE* flux in 2007 is striking and was due to higher rainfall (Table 5) and wind speeds (Table 3). More than twice as much water was evaporated from the surface in 2007 as in 2005, but the percentage of total rainfall evaporated in each year was similar (Table 5). Peak values of *LE* exceeded 1 mm evaporation per hour. Interestingly, the high *LE* flux in 2007 compensated for the low *H* flux in that year, and the combined turbulent fluxes $H + LE$ were of similar magnitude in both 2005 and 2007. Relatively high rainfall (and *LE*) totals are associated with low T_s and correspondingly low values of *H*, and vice versa.

7. Discussion

7.1. Uncertainty in the Surface Energy Balance

[42] Most of the uncertainty in the surface energy balance relates to the turbulent fluxes and *G*. *H* and *LE* are relatively insensitive to uncertainty in z_0 in the 95% confidence interval, but a doubling of z_0 increases the turbulent fluxes by about a third, implying that these fluxes would be larger over topographically rougher areas (Table 6). The impact of the assumption of similarity of z_{0t}, z_{0q} and z_{0m} on *H* and *LE* can only properly be assessed using eddy covariance measurements of vertical momentum, temperature and humidity fluxes, which are unavailable in the current study. The turbulent fluxes, in particular *H*, are very sensitive to potential temperature measurement errors (estimated as ±1°C), and *LE* is also quite sensitive to the manufacturer's quoted error in humidity measurements (Table 6). *LE* shows a very high sensitivity to *u*, implying that caution must be applied when extrapolating wind speed measurements to unmonitored sites. *G* is, relative to *H* and *LE*, fairly insensitive to T_s errors and uncertainty in K_e and *d*. The ablation stake measurements of subdebris melt rate cannot be used as an independent check on the accuracy of *G*, as they were used to estimate the K_e value applied in the conductive heat flux calculation (equation (6)).

Table 6. Sensitivity of the Sensible Heat Flux, Latent Heat Flux, and Debris Heat Flux to Uncertainty in Parameter Values and Meteorological Variables[a]

Parameter/Variable	*H* (%)	*LE* (%)	*G* (%)
$z_0 \pm 0.001$ m	−4% to +1	<±1	-
$2 \times z_0$	+32	+36	-
$T \pm 1$°C	±28	±14	-
$T_s \pm 1$°C	±28	±14	±9
$u \pm 1\% \pm 0.1$ m s^{-1}	±1	±4	-
$q \pm 3\%$	-	±10	-
$q_s \pm 4\%$	-	±17	-
$K_e \pm 10\%$	-	-	±10
$d \pm 0.01$ m	-	-	±4

[a]On the basis of likely maximum measurement errors. Values indicate the change in the mean flux values at the LWS for 2005 Given in Table 4. *H*, sensible heat flux; *LE*, latent heat flux; *G*, debris heat flux; z_0, surface roughness length (mean value = 0.016 m, 95% confidence interval = ± 0.001 m); *T,* 2 m air temperature; T_s, surface temperature; *u,* 2 m wind speed; *q* and q_s, 2 m air and surface specific humidities; K_e, debris effective thermal conductivity; *d,* debris thickness.

[43] Accurate determination of T_s and U_s is crucial for accurate estimation of the turbulent fluxes and G (and hence the subdebris ice melt rate). Direct measurement of T_s is problematic due to its high spatial variability on a rough surface subject to intense solar heating. Hence, where possible, accurate $L\uparrow$ measurements provide the best estimate of T_s as long as the surface emissivity can be estimated with sufficient accuracy. The surface emissivity value of 0.94 used in this study is supported by the close correspondence of radiative and thermistor T_s values at nighttime (Figure 2) when spatially variable solar heating effects can be ignored. Microsensors can provide sufficiently accurate U_s values for calculation of LE, but extrapolation of point measurements to the glacier-wide scale presents a challenge.

[44] A stability correction is vital to accurate calculation of the turbulent fluxes over supraglacial debris cover, due in particular to strong daytime instability in the surface layer (Figure 15). If a neutral atmosphere is assumed, the underestimation of H (Table 4) could lead to a very large overestimation of subdebris melt rates. A stability correction based on the bulk Richardson number was found to provide a successful solution to the stability problem. Neglect of a stability correction is less significant to LE because evaporation usually occurs under weakly unstable or neutral atmospheric conditions due to cloud cover, rainfall and relatively low T_s.

7.2. Distributed Modeling of the Surface Energy Balance

[45] Calculation of the $L\uparrow$, G, H and LE fluxes across a debris-covered glacier depends on the accuracy of T_s, which is in turn controlled by patterns of shortwave irradiance (shading, slope, aspect) and d. Large differences in cloud cover can occur over short distances in mountain basins, but predictable patterns also occur, e.g., the higher incidence of afternoon cloud cover at the UWS (Figure 8). Melt models driven by regional or downscaled climate model inputs can therefore benefit from periods of field-based $S\downarrow$ measurements to generate realistic cloud cover forecasts. A challenge for distributed modeling of the turbulent fluxes is the complex spatial pattern of T which is strongly influenced by T_s. For example, T will be higher over areas of thick debris, or in areas preferentially exposed to the sun. The influence of shading and aspect is more important to T differences between the LWS and UWS than elevation, resulting in a clear daily cycle in the temperature lapse rate (Figure 7). Such patterns could be used to extrapolate fields of 2 m temperature.

[46] Katabatic winds are generally absent over debris-covered areas. Instead, under fine conditions, movement of air is dominated by daytime surface convection and valley winds, which peak in intensity in late afternoon. Higher wind speeds at the LWS compared with the UWS are due to both stronger convection over the lower zone of thick debris cover and the lack of topographic sheltering from synoptic-scale pressure gradient winds. Hence, large-scale patterns of both debris thickness and surrounding mountain topography appear to be important in controlling the spatial pattern of wind speeds across a debris-covered glacier.

[47] Although it has often been neglected, determination of LE is crucial for numerical modeling of the debris surface energy balance as evaporative fluxes following rainfall are often very large (several 100 W m^{-2}) and have a depressing effect on T_s. On the other hand, energy released to the surface through condensation appears to be negligibly small. In the absence of direct measurement of U_s, the timing and volume of rainfall and the permeability of the surface need to be known to determine the availability of water for evaporation, for evaluation of LE.

7.3. Ablation of Debris-Covered Glaciers and Climate Change

[48] Calculated mean daily ice melt rates at the LWS ranged from 16 mm w.e. in 2006 to 14 mm w.e. in 2007; a difference of only 2 mm w.e. (uncertainty range 1.5–2.5 mm w.e.; Table 6) despite a mean air temperature almost one degree lower in the latter year (Table 3). Studies on debris-free glaciers indicate an ice melt rate sensitivity to a one degree temperature change about four times greater [e.g., *Braithwaite*, 2008]. This implies ablation rates beneath thick, stable debris layers will be relatively insensitive to climatic warming. This is mainly because there is no 0°C upper limit to T_s. Hence, under warm and sunny conditions, T_s rises increasing energy outputs through L and H or LE, restricting the increase in G. Cloud cover and precipitation reduce melt rates, independently of T, because surface energy input is dominated by $S\downarrow$ and energy consumed in the evaporation of surface water is very large. T_s only exceeded 25°C on days when $S\downarrow$ peaked >700 W m^{-2}. Mean S values were very similar in 2005 and 2007, but the higher LE flux in 2007 was an important factor in reducing the available melt energy by an average of 4 W m^{-2} (Table 4), equivalent to 76 mm w.e. melt over the 73 day period. Hence, increases in cloud cover and precipitation could lead to a reduction in melting of debris-covered glaciers, in spite of rising temperatures.

[49] Subdebris ice melt rates depend more strongly on debris thickness than air temperature. Studies of debris transport and trends of debris cover thickness and extent on glaciers [e.g., *Kellerer-Pirklbauer*, 2008] are therefore important for predicting the mass balance response of mountain glaciers to climate change. Crevasses and ponds create localized exposures of bare ice, which can account for a disproportionately high amount of ablation within areas of thick debris cover [e.g., *Sakai et al.*, 2002], but the controls on their development and influence on total glacier mass balance are not well known.

7.4. Debris-Covered Glacier Hydrology

[50] We estimate that 13–16% of rain falling on the debris at the LWS is evaporated back to the atmosphere (Table 5) while percolating rainwater may be temporarily stored within the debris matrix. This contrasts with debris-free temperate glaciers, where rainfall quickly enters the internal hydrological system, with minimal evaporative losses. Hence, debris covers may influence glacier hydrology and dynamics by modulating basal water pressures during high rainfall events [cf. *Mair et al.*, 2003]. However, evaporation of rainwater from debris would appear to have a small influence on catchment hydrology and downstream water resources. The mean evaporation rate of about 1 mm d^{-1} at the LWS in 2007, if extrapolated across the entire

debris covered area, would result in a reduction in runoff of just 0.06 $m^3 s^{-1}$. Further investigation of the hydrology of debris-covered glaciers and moisture fluxes between debris and the atmosphere is warranted.

8. Summary and Conclusions

[51] This study has investigated the meteorology, and quantified surface energy fluxes, on a medium-sized debris-covered glacier over three ablation seasons. Surface-layer meteorology and the debris surface energy balance are dominated by the pattern of incoming shortwave radiation which heats the debris, driving surface convection. Hence, the distribution of shading due to topography and clouds and, to an extent, aspect play an important role in spatial variations of the turbulent, outgoing longwave and debris heat fluxes and subdebris ice melt rate. The positive relationship of debris surface temperature to debris thickness means that spatial variations in debris thickness control not only variations in the subdebris ice melt rate, but also influence spatial patterns in outgoing longwave radiation, the turbulent fluxes and air temperature. One consequence is that the daytime air temperature lapse rate is very steep due to stronger daytime heating of thick debris on the lower glacier. Such clear spatial and daily patterns in meteorological variables and surface energy fluxes, related to topography and the spatial distribution of debris, could be usefully applied in distributed numerical melt models.

[52] Measured subdebris ice melt rates range from 6 to 33 mm d^{-1} for debris thickness in the range 0.55–0.04 m, and mean estimated debris thermal conductivity is 0.96 W m^{-1} K^{-1}, displaying a weak positive relationship to debris thickness. Measured bare ice melt rates are significantly higher (46–58 mm d^{-1}), indicating a critical debris thickness much less than 0.04 m.

[53] Mean seasonal values of the net shortwave, net longwave and debris heat fluxes show little variation between years, despite contrasting meteorological conditions. The increase in energy output from the debris surface in response to increasing surface temperature means that subdebris ice melt rates are fairly insensitive to variations in atmospheric temperature, in contrast to debris-free glaciers. Mean calculated subdebris melt rates were only 2 mm d^{-1} higher in 2006 compared with 2007, despite a mean temperature 0.9°C higher.

[54] Assumption of a neutral atmosphere leads to a severe underestimation of the sensible heat flux owing to strong daytime instability in the surface layer, and would lead to large errors in estimation of the subdebris ablation rate in a numerical model. A stability correction based on the Richardson number provides a simple and effective solution for bulk aerodynamic turbulent flux calculations above supraglacial debris.

[55] The latent heat flux is an important, but intermittent, energy sink. Instantaneous evaporative fluxes following rainfall can be very high if incoming shortwave radiation is strong, or when rain falls onto hot debris, but negligible if the surface is dry. Large interannual variations in the turbulent latent heat flux occur, depending on the volume and frequency of rainfall, and to an extent, wind speed. The latent heat flux was more than twice as high in the relatively wet and windy 2007 ablation season, compared with 2005. An implication is that future changes in rainfall could affect the amount of subdebris ablation due to the large amount of energy used in evaporating rainwater.

[56] The spatial distributions of debris thickness and thermal conductivity are key input fields for distributed melt modeling of debris-covered glaciers. The development of remote sensing–based debris thickness mapping techniques [e.g., *Mihalcea et al.*, 2008a, 2008b] is therefore important. To model future glacier mass balance over decadal or longer timescales, improved understanding of the controls on debris-cover formation on mountain glaciers is needed.

[57] The dependence of all surface fluxes (except net shortwave radiation and incoming longwave radiation) on debris surface temperature presents a challenge for physically based energy-balance modeling of a debris surface using meteorological measurements alone. Iterative solutions to find the unknown surface temperature value [e.g., *Nicholson and Benn*, 2006] require further development to account for instability in the surface layer. Alternatively, surface temperature may be estimated from empirical relationships to debris thickness, incoming shortwave radiation and meteorological variables [e.g., *Mihalcea et al.*, 2008b]. Modeling of the latent heat flux also requires knowledge of liquid water availability at the surface, which depends on the timing and volume of rainfall, and permeability of the debris material.

[58] There have been few micrometeorological studies of surface energy fluxes on debris-covered glaciers and similar investigations at other sites are needed to test the general validity of the findings. Eddy covariance measurements of the turbulent fluxes, and direct investigation of the spatial relationships between 2 m air and surface temperatures and debris thickness distribution would be particularly informative.

[59] **Acknowledgments.** This work was supported by NERC grant NE/C514282/1, the British Council-Italian Ministry of University and Research partnership program, and the Carnegie Trust for the Universities of Scotland. We would like to thank C. D'Agata, L. Foster, H. Maconachie, Fondazione Montagna Sicura, and the Commune of Courmayeur for logistical assistance and several undergraduate and postgraduate students from the Universities of Milan and Dundee for help with the fieldwork. T. Dixon helped in the production of the figures. The Aosta Valley Autonomy Region is thanked for supplying meteorological data. The 2005 aerial photograph in Figure 1 was provided by Regione Autonoma Valle d'Aosta. Authorization of publication N. 1375, 3.12.2009; Executed by Company Generale Ripresearee S.p.A - Parma.

References

Adhikary, S., M. Nakawo, K. Seko, and B. Shakya (2000), Dust influence on the melting process of glacier ice: Experimental results from Lirung Glacier, Nepal Himalayas, *IAHS Publ.*, *264*, 43–52.

Adhikary, S., Y. Yamaguchi, and K. Ogawa (2002), Estimation of snow ablation under a dust layer covering a wide range of albedo, *Hydrol. Process.*, *16*, 2853–2865, doi:10.1002/hyp.1075.

Arck, M., and D. Scherer (2001), A physically based method for correcting temperature data measured by naturally ventilated sensors over snow, *J. Glaciol.*, *47*, 665–670, doi:10.3189/172756501781831774.

Beniston, M. (2003), Climate change in mountain regions: A review of possible impacts, *Clim. Change*, *59*, 5–31, doi:10.1023/A:1024458411589.

Bintanja, R. (1996), The parameterization of shortwave and longwave radiation fluxes for use in zonally averaged climate models, *J. Clim.*, *9*, 439–454, doi:10.1175/1520-0442(1996)009<0439:TPOSAL>2.0.CO;2.

Bolch, T., M. Buchroithner, T. Pieczonka, and A. Kunert (2008), Planimetric and volumetric glacier changes in the Khumbu Himal, Nepal, since 1962 using Corona, Landsat TM and ASTER data, *J. Glaciol.*, *54*, 592–600, doi:10.3189/002214308786570782.

Braithwaite, R. J. (2008), Temperature and precipitation climate at the equilibrium-line altitude of glaciers expressed by the degree-day factor for melting snow, *J. Glaciol.*, *54*, 437–444, doi:10.3189/002214308785836968.

Brock, B. W., I. C. Willis, and M. J. Sharp (2006), Measurement and parameterisation of surface roughness variations at Haut Glacier d'Arolla, *J. Glaciol.*, *52*, 281–297, doi:10.3189/172756506781828746.

Brock, B., A. Rivera, G. Casassa, F. Bown, and C. Acuña (2007), The surface energy balance of an active ice-covered volcano: Volcán Villarrica, southern Chile, *Ann. Glaciol.*, *45*, 104–114, doi:10.3189/172756407782282372.

Brohan, P., J. J. Kennedy, I. Harris, S. F. B. Tett, and P. D. Jones (2006), Uncertainty estimates in regional and global observed temperature changes: A new dataset from 1850, *J. Geophys. Res.*, *111*, D12106, doi:10.1029/2005JD006548.

Brutsaert, W. (1982), *Evaporation Into the Atmosphere: Theory, History and Applications*, 299 pp., Springer, New York.

Conway, H., and L. A. Rasmussen (2000), Summer temperature profiles within supraglacial debris on Khumbu Glacier, Nepal, *IAHS Publ.*, *264*, 89–97.

Deline, P. (2005), Change in surface debris cover on Mont Blanc massif glaciers after the "Little Ice Age" termination, *Holocene*, *15*, 302–309, doi:10.1191/0959683605hl809rr.

Deline, P. (2009), Interactions between rock avalanches and glaciers in the Mont Blanc massif during the late Holocene, *Quat. Sci. Rev.*, *28*, 1070–1083, doi:10.1016/j.quascirev.2008.09.025.

Denby, B., and W. Greuell (2000), The use of bulk and profile methods for determining surface heat fluxes in the presence of glacier winds, *J. Glaciol.*, *46*, 445–452, doi:10.3189/172756500781833124.

Diolaiuti, G., C. D'Agata, A. Meazza, A. Zanutta, and C. Smiraglia (2009), Recent (1975–2003) changes in the Miage debris-covered glacier tongue (Mont Blanc, Italy) from analysis of aerial photos and maps, *Geogr. Fis. Dinam. Quat.*, *32*, 117–127.

Dozier, J., and J. Frew (1990), Rapid calculation of terrain parameters for radiation modeling from digital elevation data, *IEEE Trans. Geosci. Remote Sens.*, *28*, 963–969, doi:10.1109/36.58986.

Favier, V., P. Wagnon, J.-P. Chazarin, L. Maisincho, and A. Coudrain (2004), One-year measurements of surface heat budget on the ablation zone of Antizana Glacier 15, Ecuadorian Andes, *J. Geophys. Res.*, *109*, D18105, doi:10.1029/2003JD004359.

Fujita, K., and A. Sakai (2000), Air temperature environment on the debris-covered area of Lirung Glacier, Langtang Valley, Nepal Himalayas, *IAHS Publ.*, *264*, 83–88.

Georges, C., and G. Kaser (2002), Ventilated and unventilated air temperature measurements for glacier-climate studies on a tropical high mountain site, *J. Geophys. Res.*, *107*(D24), 4775, doi:10.1029/2002JD002503.

Greuell, W., and C. Genthon (2004), Modelling land-ice surface mass balance, in *Mass Balance of the Cryosphere: Observations and Modelling of Contemporary and Future Changes*, edited by J. L. Bamber and A. J. Payne, pp. 117–168, Cambridge Univ. Press, New York.

Greuell, W., W. H. Knap, and P. C. Smeets (1997), Elevational changes in meteorological variables along a midlatitude glacier during summer, *J. Geophys. Res.*, *102*, 25,941–25,954, doi:10.1029/97JD02083.

Hagg, W., C. Mayer, A. Lambrecht, and A. Helm (2008), Sub-debris melt rates on southern Inylchek Glacier, central Tian Shan, *Geogr. Ann., Ser. A.*, *90*, 55–63, doi:10.1111/j.1468-0459.2008.00333.x.

Hartmann, D. L. (1994), *Global Physical Climatology*, 411 pp., Academic, London.

Hewitt, K., C. P. Wake, G. J. Young, and C. David (1989), Hydrological investigations at Biafo Glacier, Karakoram Himalaya: An important source of water for the Indus River, *Ann. Glaciol.*, *13*, 103–108.

Hock, R. (2005), Glacier melt: A review of processes and their modeling, *Prog. Phys. Geogr.*, *29*, 362–391, doi:10.1191/0309133305pp453ra.

Hoffman, M. J., A. G. Fountain, and G. E. Liston (2008), Surface energy balance and melt thresholds over 11 years at Taylor Glacier, Antarctica, *J. Geophys. Res.*, *113*, F04014, doi:10.1029/2008JF001029.

Kayastha, R. B., Y. Takeuchi, M. Nakawo, and Y. Ageta (2000), Practical prediction of ice melting beneath various thickness of debris cover on Khumbu Glacier, Nepal, using a positive degree-day factor, *IAHS Publ.*, *264*, 71–82.

Kellerer-Pirklbauer, A. (2008), The supraglacial debris-system at the Pasterze Glacier, Austria: Spatial distribution, characteristics and transport of debris, *Z. Geomorphol.*, *52*, 3–25, doi:10.1127/0372-8854/2008/0052S1-0003.

Kirkbride, M. P. (2010), Debris-covered glaciers, in *Encyclopedia of Snow, Ice and Glaciers*, edited by U. K. Haritashya, P. Singh, and V. P. Singh, Springer, New York, in press.

Kirkbride, M. P., and A. J. Dugmore (2003), Glaciological response to distal tephra fallout from the 1947 eruption of Hekla, south Iceland, *J. Glaciol.*, *49*, 420–428, doi:10.3189/172756503781830575.

Lide, D. R. (Ed.) (2004), *CRC Handbook of Chemistry and Physics*, 85th ed., CRC Press, Boca Raton, Fla.

Mair, D., I. Willis, U. H. Fischer, B. Hubbard, P. Nienow, and A. Hubbard (2003), Hydrological controls on patterns of surface, internal and basal motion during three "spring events": Haut Glacier d'Arolla, Switzerland, *J. Glaciol.*, *49*, 555–567, doi:10.3189/172756503781830467.

Mattson, L. E., and J. S. Gardner (1989), Energy exchange and ablation rates on the debris-covered Rakhiot Glacier, Pakistan, *Z. Gletscherkd. Glazialgeol.*, *25*, 17–32.

Mayer, C., A. Lambrecht, M. Belò, C. Smiraglia, and G. Diolaiuti (2006), Glaciological characteristics of the ablation zone of Baltoro Glacier, Karakoram, *Ann. Glaciol.*, *43*, 123–131, doi:10.3189/172756406781812087.

Mihalcea, C., C. Mayer, G. Diolaiuti, A. Lambrecht, C. Smiraglia, and G. Tartari (2006), Ice ablation and meteorological conditions on the debris covered area of Baltoro Glacier (Karakoram, Pakistan), *Ann. Glaciol.*, *43*, 292–300, doi:10.3189/172756406781812104.

Mihalcea, C., B. W. Brock, G. Diolaiuti, C. D'Agata, M. Citterio, M. P. Kirkbride, M. E. J. Cutler, and C. Smiraglia (2008a), Using ASTER satellite and ground-based surface temperature measurements to derive supraglacial debris cover and thickness patterns on Miage Glacier (Mont Blanc Massif, Italy), *Cold Reg. Sci. Technol.*, *52*, 341–354, doi:10.1016/j.coldregions.2007.03.004.

Mihalcea, C., C. Mayer, G. Diolaiuti, C. D'Agata, C. Smiraglia, A. Lambrecht, E. Vuillermoz, and G. Tartari (2008b), Spatial distribution of debris thickness and melting from remote-sensing and meteorological data, at debris-covered Baltoro Glacier, Karakoram, Pakistan, *Ann. Glaciol.*, *48*, 49–57, doi:10.3189/172756408784700680.

Mölg, T., and D. R. Hardy (2004), Ablation and associated energy balance of a horizontal glacier surface on Kilimanjaro, *J. Geophys. Res.*, *109*, D16104, doi:10.1029/2003JD004338.

Moore, R. D. (1983), On the use of bulk aerodynamic formulae over melting snow, *Nord. Hydrol.*, *14*, 193–206.

Munro, D. S. (1989), Surface roughness and bulk heat transfer on a glacier: Comparison with eddy correlation, *J. Glaciol.*, *35*, 343–348.

Nakawo, M., and G. J. Young (1981), Field experiments to determine the effect of a debris layer on ablation of glacier ice, *Ann. Glaciol.*, *2*, 85–91.

Nakawo, M., and G. J. Young (1982), Estimate of glacier ablation under a debris layer from surface temperature and meteorological variables, *J. Glaciol.*, *28*, 29–34.

Nicholson, L., and D. I. Benn (2006), Calculating ice melt beneath a debris layer using meteorological data, *J. Glaciol.*, *52*, 463–470, doi:10.3189/172756506781828584.

Oke, T. R. (1987), *Boundary Layer Climates*, 2nd ed., 435 pp., Routledge, New York.

Østrem, G. (1959), Ice melting under a thin layer of moraine and the existence of ice cores in moraine ridges, *Geogr. Ann., Ser. A*, *41*, 228–230.

Pellicciotti, F., B. W. Brock, U. Strasser, P. Burlando, M. Funk, and J. Corripio (2005), An enhanced temperature-index glacier melt model including the shortwave radiation balance: Development and testing for Haut Glacier d'Arolla, Switzerland, *J. Glaciol.*, *51*, 573–587, doi:10.3189/172756505781829124.

Popovnin, V. V., and A. Rozova (2002), Influence of sub-debris thawing on ablation and runoff of the Djankuat Glacier in the Caucasus, *Nord. Hydrol.*, *33*, 75–94.

Rana, B., M. Nakawo, Y. Fukushima, and Y. Ageta (1997), Application of a conceptual precipitation–runoff model (HYCYMODEL) in a debris-covered glacierized basin in the Langtang Valley, Nepal Himalaya, *Ann. Glaciol.*, *25*, 226–231.

Robinson, E. S., and C. Coruh (1988), *Basic Exploration Geophysics*, John Wiley, New York.

Sakai, A., M. Nakawo, and K. Fujita (2002), Distribution characteristics and energy balance of ice cliffs on debris-covered glaciers, Nepal Himalaya, *Arct. Antarct. Alp. Res.*, *34*, 12–19, doi:10.2307/1552503.

Sicart, J. E., P. Wagnon, and P. Ribstein (2005), Atmospheric controls on the heat balance of Zongo Glacier (16°S, Bolivia), *J. Geophys. Res.*, *110*, D12106, doi:10.1029/2004JD005732.

Singh, P., M. Arora, and N. K. Goel (2006), Effect of climate change on runoff of a glacierized Himalayan basin, *Hydrol. Process.*, *20*, 1979–1992, doi:10.1002/hyp.5991.

Stokes, C. R., V. Popovnin, A. Aleynikov, S. D. Gurney, and M. Shahgedanova (2007), Recent glacier retreat in the Caucasus Mountains, Russia, and associated increase in supraglacial debris cover and supra-/proglacial

lake development, *Ann. Glaciol.*, *46*, 195–203, doi:10.3189/172756407782871468.

Strasser, U., J. Corripio, F. Pellicciotti, P. Burlando, B. Brock, and M. Funk (2004), Spatial and temporal variability of meteorological variables at Haut Glacier d'Arolla (Switzerland) during the ablation season 2001: Measurements and simulations, *J. Geophys. Res.*, *109*, D03103, doi:10.1029/2003JD003973.

Takeuchi, Y., R. B. Kayastha, and M. Nakawo (2000), Characteristics of ablation and heat balance in debris-free and debris-covered areas on Khumbu Glacier, Nepal Himalayas, in the pre-monsoon season, *IAHS Publ.*, *264*, 53–61.

Van de Wal, R. S. W., W. Greuell, M. R. Van den Broeke, C. J. Reijmer, and J. Oerlemans (2005), Surface mass-balance observations and automatic weather station data along a transect near Kangerlussuaq, west Greenland, *Ann. Glaciol.*, *42*, 311–316, doi:10.3189/172756405781812529.

Viviroli, D., H. H. Dürr, B. Messerli, and M. Meybeck (2007), Mountains of the world, water towers for humanity: Typology, mapping, and global significance, *Water Resour. Res.*, *43*, W07447, doi:10.1029/2006WR005653.

B. W. Brock, M. E. J. Cutler, and M. P. Kirkbride, School of Social and Environmental Sciences, University of Dundee, Dundee DD1 4HN, UK. (b.w.brock@dundee.ac.uk)

G. Diolaiuti, C. Mihalcea, and C. Smiraglia, Department of Earth Sciences, University of Milan, Via Mangiagalli 34, Milan, I-20133, Italy.